metals

MDPI

Article

Influence of Tool–Base Metal Interference on the Performance of an Aluminium–Magnesium Alloy Joined via Bobbin Tool Friction Stir Welding

Sebastian Balos [1], Danka Labus Zlatanovic [1,2], Nenad Kulundzic [1], Petar Janjatovic [1], Miroslav Dramicanin [1], Zorana Lanc [1], Miodrag Hadzistevic [1], Slobodan Radisic [3,4,*], Dragan Rajnovic [1] and Milan Pecanac [1,*]

[1] Department of Production Engineering, Faculty of Technical Sciences, University of Novi Sad, 21000 Novi Sad, Serbia; sebab@uns.ac.rs (S.B.); danlabus@uns.ac.rs (D.L.Z.); kulundzic@uns.ac.rs (N.K.); janjatovic@uns.ac.rs (P.J.); dramicanin@uns.ac.rs (M.D.); zoranalanc@uns.ac.rs (Z.L.); miodrags@uns.ac.rs (M.H.); draganr@uns.ac.rs (D.R.)
[2] Department of Production Technology, Technische Universität Ilmenau, 98693 Ilmenau, Germany
[3] Faculty of Technical Sciences, University of Novi Sad, 21000 Novi Sad, Serbia
[4] Faculty of Economics and Engineering Management, University Business Academy Novi Sad, 21107 Novi Sad, Serbia
* Correspondence: sradisic@uns.ac.rs (S.R.); pecanac.milan@uns.ac.rs (M.P.); Tel.: +381-21-4852435 (S.R.); +381-21-4852322 (M.P.)

Abstract: Bobbin tool friction stir welding (BTFSW) is a variant of the FSW process which uses the special two-shoulder tool that forms the top and bottom of a weld surface. As such, a significant simplification of the welding setup is achieved. One of the dominant parameters of the BTFSW process is the interference between the tool shoulder pinch gap and the weld metal thickness. In this research, the influence of interference of the square pin tool with convex shoulders on process temperature, microstructure, tensile, impact, and bend performance were studied, and appropriate correlations were devised. The base metal was an aluminum–magnesium alloy in which the interference varied in the range of 0.1 to 0.5 mm. Wormhole defects and irregularities were found in all specimens except in the specimen welded with 0.4 mm interference. An optimal interference of 0.4 mm resulted in the best mechanical properties, which, in terms of tensile strength and reduction of area, were similar to the base metal. Furthermore, the impact strength was significantly higher, which was attributed to the grain refinement effect in the nugget zone.

Keywords: bobbin tool; friction stir welding; interference; mechanical properties; microstructure; fracture surface

Citation: Balos, S.; Labus Zlatanovic, D.; Kulundzic, N.; Janjatovic, P.; Dramicanin, M.; Lanc, Z.; Hadzistevic, M.; Radisic, S.; Rajnovic, D.; Pecanac, M. Influence of Tool–Base Metal Interference on the Performance of an Aluminium–Magnesium Alloy Joined via Bobbin Tool Friction Stir Welding. *Metals* **2023**, *13*, 1215. https://doi.org/10.3390/met13071215

Academic Editor: Sergey Malopheyev

Received: 17 May 2023
Revised: 16 June 2023
Accepted: 23 June 2023
Published: 30 June 2023

1. Introduction

Friction stir welding (FSW) was patented at The Welding Institute (TWI) in the UK. Since its invention in 1991, a significant development effort has been conducted in order to adapt this process in order to make it suitable for welding various materials and geometries, in different positions and joint types, while producing joints with reduced or eliminated imperfections and defects [1,2]. Developments have thus gone in several directions. It has been mainly directed towards the development of tool geometry and experimental set-up. For example, complex kinematic patterns have been applied in reversal stir welding or re-stir [3], where the majority of problems associated with the inherent asymmetry of the conventional FSW are avoided. Complex tool geometries, stationary and semi-stationary tools have also been also used. Stationary-shoulder FSW (SSFSW) provides relatively uniform and balanced heat input through the thickness of a base metal, suppressing defects and, at the same time, improving the microstructural and mechanical properties of welds [4]. Furthermore, the semi-stationary-shoulder tool FSW influences the movement of defects

close to the base material's surface, where they are easily detected and are capable of being removed [5]. Furthermore, allied technologies have emerged: friction stir processing (FSP), channeling/tunnelling (FSC/FST), incremental forming (FSIF), riveting (FSR), and extrusion (FSE), all of which explore the same concept of material-friction-based heating using an optimized tool and stirring it in order to obtain technological benefits other than welding [6]. Friction stir processing deals with microstructural modification, which is beneficial to the enhancement of material properties [7,8]. Friction stir channeling/tunneling was developed to produce a subsurface internal closed channel in a monolithic plate with no limitations in length and direction, enabling the fabrication of lightweight, structurally stiff panels and highly efficient thermal management systems [9,10]. Friction stir incremental forming is a process that combines FSW and incremental sheet-metal-forming [11,12]. Friction stir-riveting combines the spinning and extruding actions of FSW, and the interlocking by embedding a rivet in making a joint [13,14]. Friction stir extrusion is a direct-recycling technology, wherein a rotating die is plunged into a cylindrical chamber containing recycling material, usually machining chips [15].

Advantages of well-designed, FSW-based processes are solid joints without heat induced defects such as pores and hot cracks; lower distortion and shrinkage; and superior mechanical properties compared to fusion-based processes, particularly in the joining of difficult-to-weld materials and dissimilar materials. Furthermore, no filler, flux, or shielding gases are needed, and the technology is energy-efficient and environmentally friendly. The disadvantages include the high cost of specialized equipment, lower flexibility compared to arc-welding processes, non-forgeable materials that cannot be joined, and complex special fixtures including a backing plate [16–18]. Bobbin tool FSW (BTFSW) was envisaged as a simplified (and thus, more reliable) process, using a special two-sided shoulder tool interconnected via a probe (Figure 1a), enveloping the base metal from the top and bottom, eliminating the vertical force needed during conventional FSW (Figure 1b). This way, root imperfections may also be avoided, theoretically improving the bend and fatigue performance of welds [1,19].

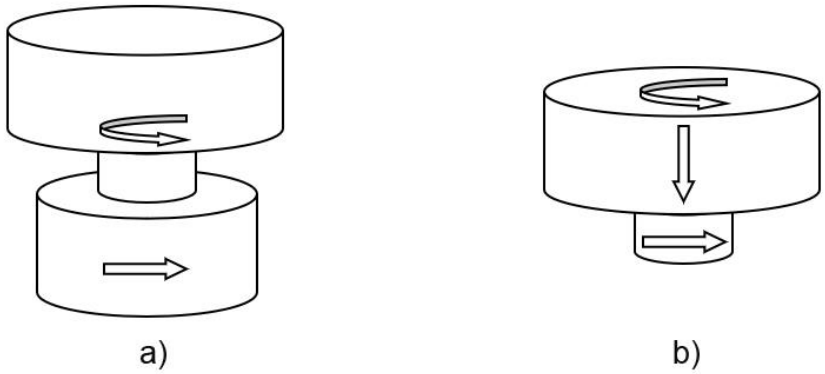

Figure 1. Schematic of FSW tools: (**a**) bobbin tool; (**b**) conventional.

Other advantages of BTFSW were identified as higher and more balanced heat input to both sides of the weld with less distortion, and successful welding of closed, hollow, extruded profiles [19]. However, the tool probe undergoes tensile, torsion, and bending forces significantly greater than those encountered by a conventional FSW tool probe, which undergoes compression, torsion, and bending [20]. Tensile stresses in the probe are highly dependent on tool geometry and welding parameters, in which interference can be viewed as equivalent to plunging depth in conventional FSW. Interference that is too low has a similar effect to a lower plunge depth: a possible insufficient forging effect, friction, and heat generation, leaking of the material from the weld zone, and possible defects. On the other hand, a smaller shoulder gap (too much interference) is the equivalent of a larger plunge depth, generating more friction and heat, but also more flash and stress, leading to a shorter tool life due to probe fracture [19].

Okamoto et al. [21] developed a tool with a convex scroll shoulder and a thread pin with three flats for the welding of an AA6068–T6 alloy, to achieve a joint efficiency of 68%. Sued and Pons [22] reported that a greater interference when using bobbin-tool FSW on an AA6068–T6 resulted in a defect-free joint. Two tools were used, one with scrolled shoulders/a cylindrical probe and the other, a cylindrical tool with a flat shoulder and a probe with three flats. The simple cylindrical probe tool proved to be unsatisfactory. Better results were obtained with the more complex tool with flats, or in other words, a tool probe with a triangular cross-section and rounded edges. The same tools also proved to be superior in the work of Suad et al. [23], who reported that, when welding a 4 mm AA6082–T6 via BTFSW, the medium 3.75% interference was optimal, despite the existence of a moderate close tunnel defect. A 0% interference resulted in closed-tunnel, open-void, and groove defects, while an 8.75% interference caused open tunnels combined with a few closed tunnels, which were combined with high generated forces in the tool. Zhang et al. [24] also applied a scrolled shoulder and a cylindrical probe with three flats and a plunge depth of 0.07 mm at each side of the base metal, effectively resulting in 2.3% interference at each side of the base metal, to weld a 6 mm 2A14–T6 alloy and reach a joint efficiency of 75%. Most of the previous research consists of an investigation of the influence of tool geometry and tool interference during BTFSW on the tensile strength and hardness of the joins. However, there is a limited amount of research dealing with the influence of BTFSW geometry (especially interference) on impact strength and bending properties, which are expected to be better compared to FSW joints because the material flow which envelops the metal from the top and bottom and the typical notch, which can be found in conventional friction stir welds on the bottom side, is avoided.

In this work, the influence of interference from a square pin tool with convex shoulders on mechanical properties, namely, impact and tensile strength, bending properties, and joint efficiency, was investigated. Furthermore, macro- and microstructural features were studied as well, in order to correlate the mechanical properties with the grain size and to analyze process defects. Furthermore, there is an interest in designing a tool with simpler geometry, without complex features, which is easier to clean, and which will further the industrial potential of the relatively simple BTFSW layout.

2. Materials and Methods

For the purpose of the experimental investigation, AA5005 H32 aluminum–magnesium alloy was used. Chemical composition was tested via ARL 3580 (Thermo Scientific, Waltham, MA, USA) optical emission spectrometer (OES) and tensile mechanical properties were obtained via ZDM 5/91 (VEB, Leipzig, Germany) tensile testing machine and are presented in Tables 1 and 2, respectively.

Table 1. Chemical composition of the base material [mass. %].

%	Cu	Mn	Mg	Si	Fe	Zn	Ti	Al
Base material	0.05	0.12	0.6	0.22	0.29	0.06	0.017	Balance

Table 2. Mechanical properties of the base material.

Rp MPa	Rm MPa	A%	Z%
120	135	15	60

The experimental welding was performed on a FSSGVK-3 (Prvomajska, Zagreb, Croatia) vertical milling machine, with a specially designed fixture (Figure 2) for providing stable butt-welding conditions of 150 × 60 × 5 mm plates. BTFSW tool temperature was monitored by using the IR camera, TP8S (ThermoPro, Toronto, Canada), with a temperature range from −20 °C to 2000 °C, accuracy of ±2 °C, and coefficient of emissivity of 0.4.

The clamping system provided the central groove that allows the passage of the bottom shoulder of the tool without interference. An array of tools was designed, having both shoulders with a convex shape with a dip angle of 2°, while the pin was of four-sided flat type, with the geometry shown in Figure 3. Tool geometry was designed to have key working surfaces easily accessible and simple for cleaning (no scrolls, as in [14]), and therefore, to be well suited for industrial use. The tool material was AISI H13 (X40CrMoV5-1) hot-work tool steel, quenched in oil and tempered to 53 HRC. Welding parameters and designation system are given in Table 3. The distance between tool shoulders was varied, influencing the interference and therefore, the forging effect within the base material, in order to determine its influence on mechanical properties and microstructural features of welds.

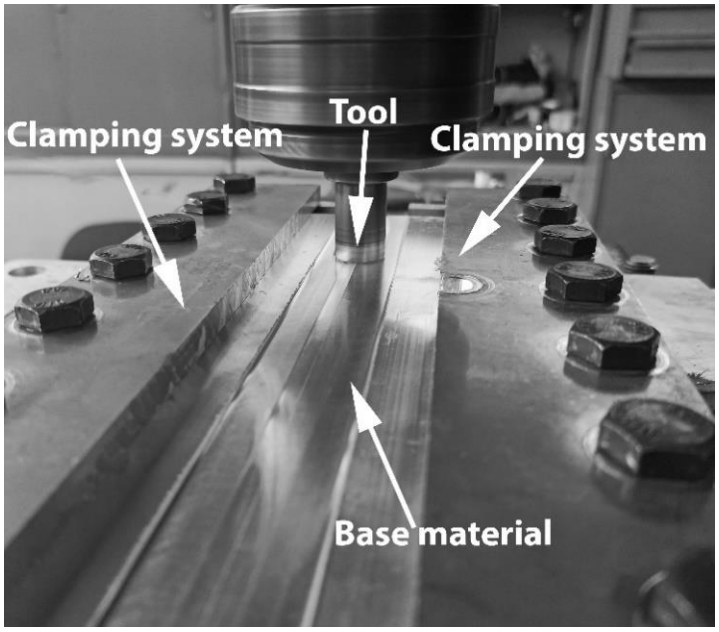

Figure 2. Fixture used in the experimental work.

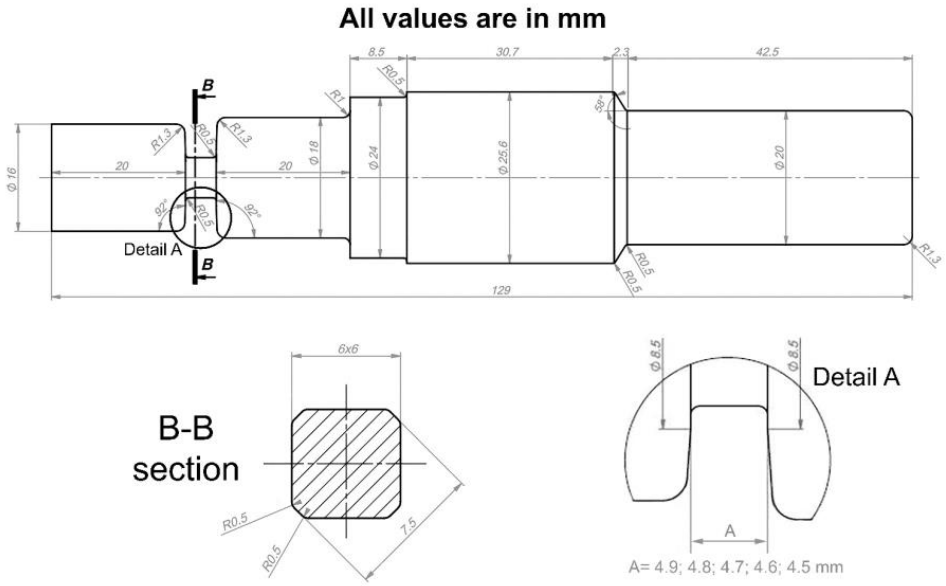

Figure 3. Tool geometry.

Table 3. Experiment designation system.

Weld Designation	Shoulder Pinch Gap at the Periphery mm	Interference mm	Interference %	Tool Rotation Speed rpm	Welding Speed mm/min
1	4.9	0.1	2		
2	4.8	0.2	4		
3	4.7	0.3	6	1400	20
4	4.6	0.4	8		
5	4.5	0.5	10		

Weld characterization comprised tensile, bend, and impact testing, and macro and microstructural analysis was also conducted. Tensile testing was performed on VEB ZDM 5/91 (Verkstoffpruefmaschinen, Leipzig, Germany) mechanical tensile testing machine, complying with EN ISO 4136:2012 standard on two specimens. Ultimate tensile strength and cross-section reduction were reported, as well as joint efficiencies. Charpy impact test was performed on JWT-450 (Jinan, China) instrumented tester at room temperature, in accordance with EN ISO 148-1:2016 standard on two specimens. V-notch was machined so that the crack initiation and propagation passed through the nugget zone (NZ). Bend testing was also performed on VEB ZDM 5/91 machine, in accordance with EN ISO 5173:2009 standard. It was performed on four specimens, two bent one over the top, the other over the bottom of the weld. Three-point bending was conducted until a crack appeared on the surface of the sample and the average angle was reported. Afterwards, the testing continued until fracture, or until reaching the full 180°.

Standard metallographic preparation was performed, comprising grinding with SiC abrasive papers (220 to 2500 grit), polishing with diamond suspension (6, 3, 1 and $\frac{1}{4}$ µm diamond particles), and OP-S colloidal silica suspension. Etching was performed using anodic oxidation process in Barker's reagent (5 mL HBF4 + 200 mL distilled water). Welds were examined using Leitz Orthoplan (Leica, Wetzlar, Germany) light microscope under polarized light. Grain size was determined via comparison procedure, using ASTM E112 standard. Fracture surfaces were assessed via JEOL JSM-6460LV scanning electron microscope (SEM), operating at 20 kV, while energy-dispersive X-ray analysis was performed using Oxford Instruments INCA microanalysis systems. Mechanical testing results were correlated to macro, micro examination, including grain size, as well as maximal tool temperatures obtained from thermograms.

3. Results

3.1. Thermograms

Thermograms of the BTFSW tool are shown in Figure 4. As can be seen, the maximal measured temperatures are on the tool near to the base material. The depicted thermograms show the top shoulder, as the bottom shoulder is within the groove of the fixture and therefore, line-of-sight is not provided. In some specimens, the tool surroundings show relatively high temperatures, higher than the actual ones, due to the highly reflective aluminum surface. The maximal temperature was measured at the tool, providing the highest interference between the top shoulder and base metal (Figure 4e). This was due to the highest pressure in the material having been induced by BTFSW tool shoulders. In addition to this, the tool had a longer contact with the base material, which induced this relatively high temperature. This is analogous to the increase in welding speed or rotational speed, as in [6].

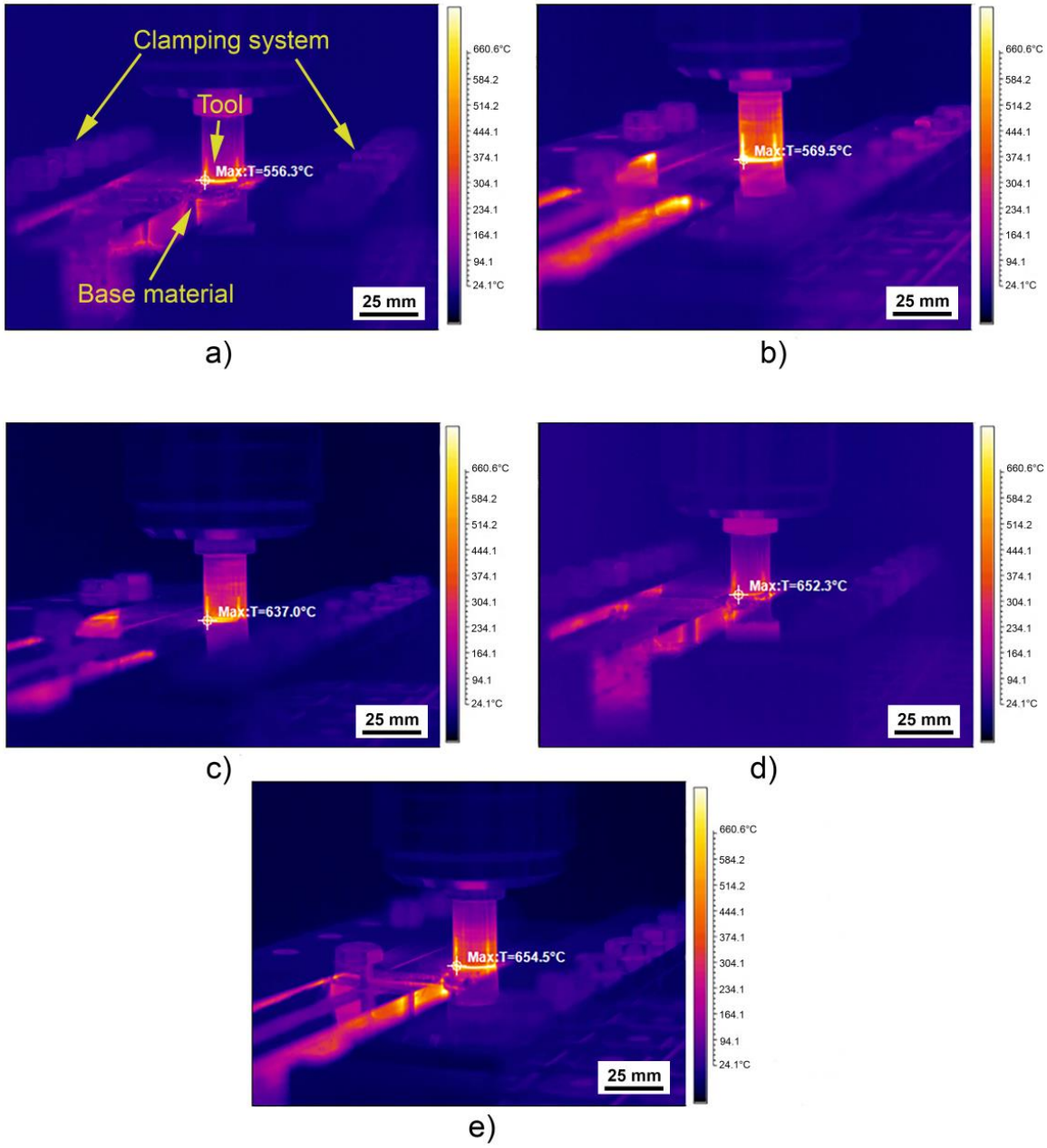

Figure 4. Thermograms with peak tool temperature: (**a**) Specimen 1; (**b**) Specimen 2; (**c**) Specimen 3; (**d**) Specimen 4; (**e**) Specimen 5.

3.2. Metallographic Testing Results

Macro cross-sections of welds obtained with different interferences are shown in Figure 5. A higher interference causes a more pronounced flash to occur, indicated by the black arrows. Wormhole defects (ISO 6520-1 reference number 200) were present in all specimens except Specimen 4 with the interference of 0.4 mm. Wormholes are shown in the form of white areas, indicated by white arrows. The wormhole defects occurred within the waist formed by the tool (thermo-mechanically affected zone/nugget zone), towards the advancing side (AS). In Specimen 1, with the highest interference, the wormhole protruded into the nugget. In Specimen 2, multiple wormholes were observed, some also within the nugget. This can be viewed as a transition towards a single triangular wormhole combined with a narrow crack-like one in Specimen 3. In Specimen 5, a single triangular wormhole was present. Maximal wormhole dimensions are shown in Table 4, as well as the compliance with ISO 25239-5 standard [25]. That means, the applied technology,

comprising the tool geometry and welding kinematic parameters can be utilized to obtain BTFSW welds that fully comply with acceptance level B (Specimen 4) and acceptance level C (Specimens 3 and 5), indicating that Specimens 3, 4, and 5 were suitable for industrial use, where Specimen 4 is compliant with the most stringent conditions. Root imperfections were not present, as BTFSW eliminates them through the existence of double shoulders, except for open tunnels, which can occur at both sides of the weld [26].

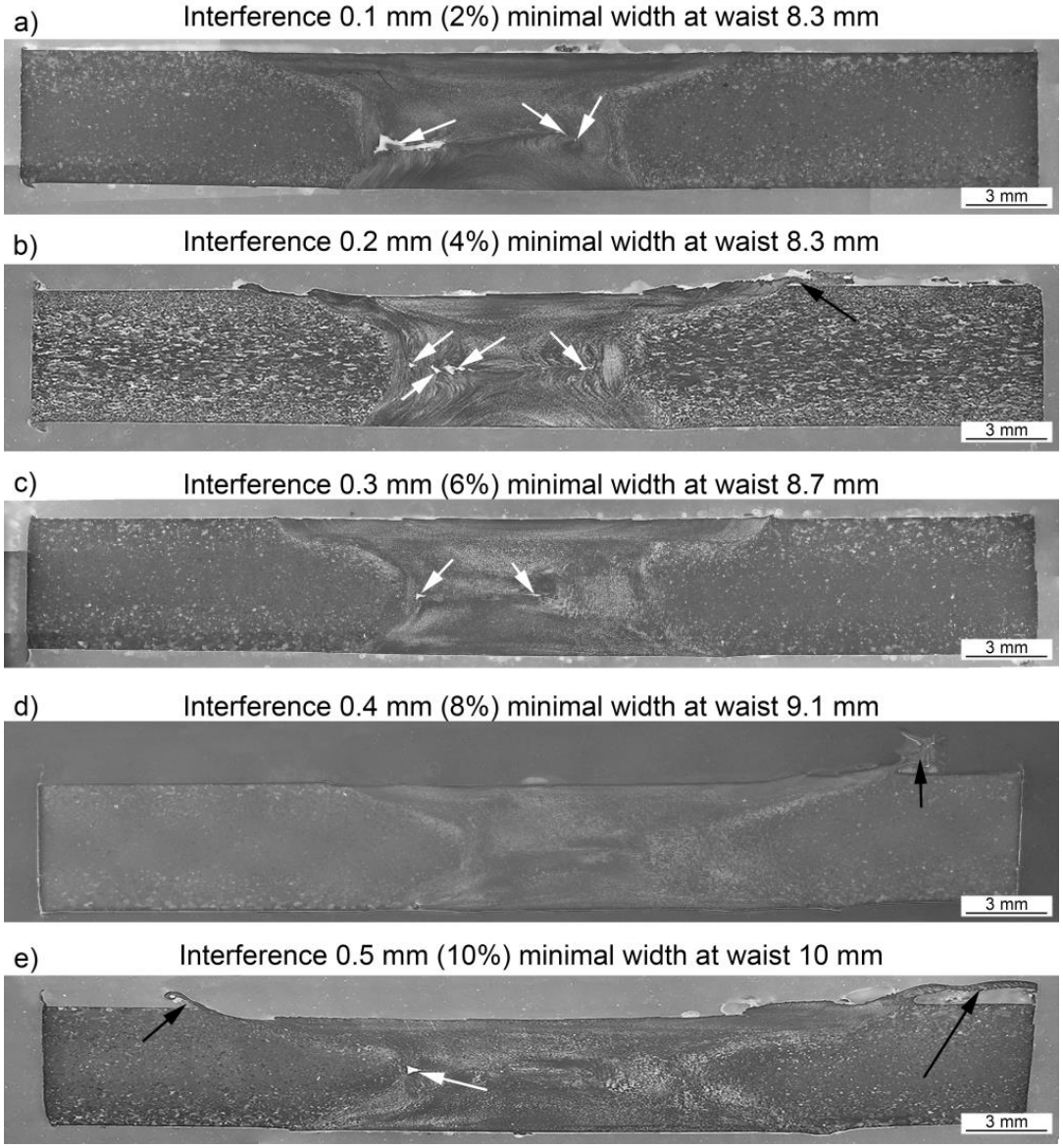

Figure 5. Weld macro images: (**a**) Specimen 1; (**b**) Specimen 2; (**c**) Specimen 3; (**d**) Specimen 4; (**e**) Specimen 5.

Table 4. Wormhole dimensions and compliance with ISO 25239-5 standard.

Specimen	Cavity Width × Height [mm]	Acceptance Level-ISO 25239-5 Standard
1	2.48 × 0.8	Not compliant
2	2.37 × 0.27; 0.03 × 0.03	Not compliant
3	0.04 × 0.04; 0.07 × 0.01	C
4	0	B
5	0.04 × 0.4	C

A higher interference influences a rise in the maximum temperature of the tool due to increased friction. A higher temperature softens the material more intensively, causing a rise in minimal width at the waist in macro images (minimal distance between TMAZ-AS/HAZ interface to TMAZ-RS/HAZ interface), Figure 5. The dependence of minimal width at the waist from interference is shown in Figure 6. The obtained coefficient of determination of the fitted curve $R^2 = 0.99374$ is relatively high, proving that the proposed fitting regression quadratic polynomial function line approximates the actual data well, for the purpose of interpolation. The trend of width at the waist (in relation to interference-induced maximal process temperature) behaves similarly to the width of NZ and TMAZ zones (in relation to tool-rotation-speed-induced process temperature) in friction-stir-spot-welded Al–Mg specimens obtained in [27].

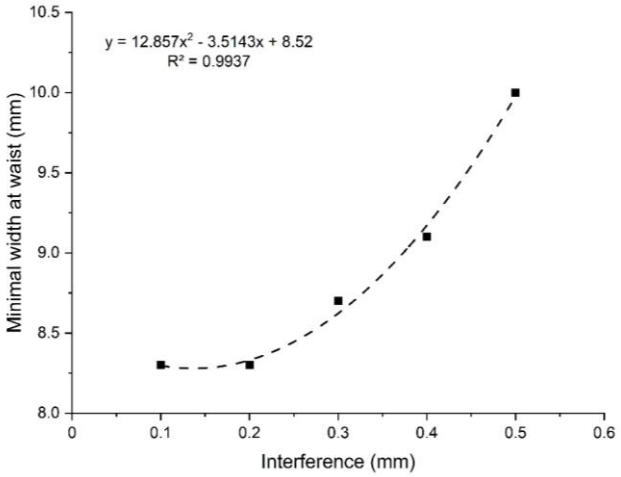

Figure 6. Minimal width at waist vs. interference.

In Specimen 1, with the lowest interference, the minimal width-at-waist was just slightly higher than the maximal dimension of the pin (7.5 mm, Figure 2). As the interference decreased, the stir zone became more cylindrical. An increased interference and subsequent increased tool temperature inevitably increase stresses in the material and potentially reduce tool life [28].

The shape of the NZ/TMAZ as the interference increased, appeared more dumb-bell-shaped, with a shaper, more pronounced curvature towards the central section. This effect is similar to the effect of decreasing the welding speed, which is in accordance with the work of Zhang et al. [24]. It can be attributed to the increased stirring effect that comes from the shoulder surfaces. Furthermore, the interface between the dumb-bell-shaped area and the HAZ was much sharper on the AS, while it was rather unclear on the RS. This phenomenon was reported by Dickerson and Przydatek [29], Leonard and Lockyer [30], and Treadgyll et al. [31].

Metallographic images of the base material, HAZ, and nugget are shown in Figure 7. HAZ (7a; 7b, 7c) and nugget (7d; 7e; 7f) microstructures were reported for the most representative specimens, such as Specimen 1 (the lowest interference), Specimen 4 (optimal), and Specimen 5 (the highest interferences). The white circle in Figure 5a indicates the position where the HAZ and nugget microstructures in Figure 7a–f were taken. Average grain size (G) and the corresponding average diameters in these zones are shown in Table 5 according to standard ASTM E112. Base metal consists of uniaxial grains with an average size of 4.5. As the interference becomes higher, the grains are coarser in the nugget zone. The key reason for this behavior is the greater heat generated by a more pronounced interference between the tool shoulder pinching gap and the thickness of the base metal, as shown by the listed thermograms in Figure 4. The higher squeezing effect, that is, deformation, when greater interference was present suggests that more refined grains should have been obtained in NZ. However, this was not the case, as a higher

temperature generated during the BTFSW process overcomes this higher strain. In HAZ, a similar trend was observed, where a higher heat input induced grain coarsening through recrystallization. HAZ undergoes a thermal cycle only, that is, a higher heat generation in specimens welded with higher-interference tools. These results can be well correlated to the results reported by Shen et al. [32]. At the lowest interference (Specimen 1), just a slight difference between HAZ and BM grain size was present, due to the minimal thermal effect, which was also found by Sahu et al., who also applied a relatively low welding speed of the same order [33].

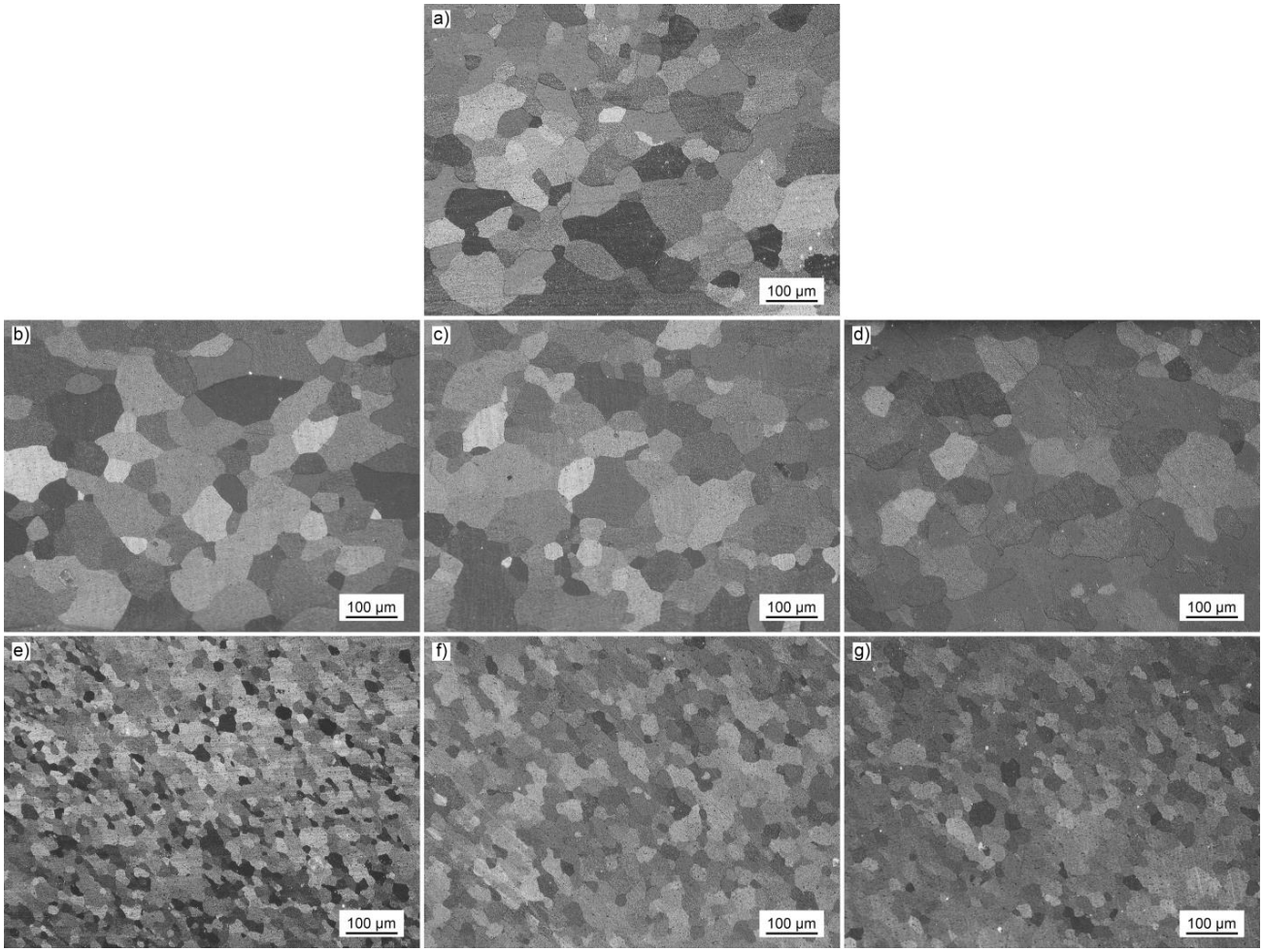

Figure 7. Microstructures of (**a**) base material; HAZ: (**b**) Specimen 1; (**c**) Specimen 4; (**d**) Specimen 5; nugget zone: (**e**) Specimen 1; (**f**) Specimen 4; (**g**) Specimen 5.

Table 5. Average grain sizes according to ASTM E112.

Specimen	HAZ		NZ	
	Grain Size No. G	Average Diameter [µm]	Grain Size No. G	Average Diameter [µm]
1	4	89.8	10	11.2
2	3	127	9	15.9
3	3	127	8.5	18.9
4	2.5	151	7.5	26.7
5	2.5	151	7	31.8

3.3. Tensile Testing Results

Tensile testing results are shown in Figure 8. The highest tensile strength was obtained in Specimen 4, which can be attributed to the absence of a wormhole defect. A lower degree of interference results in a lower peak temperature and therefore, a less pronounced grain coarsening in the HAZ (Specimens 1–3). On the other hand, an increased degree interference induced elevated welding temperatures, which caused a grain-coarsening effect in the HAZ, which, along with the presence of a wormhole defect, resulted in a relatively low tensile strength (Specimen 5). In Figure 9, stress–strain charts of BM, Specimens 4 and 5 are shown. Specimen 4 and 5's stress–strain curves are similar to the BM, depicting typical ductile behavior. In Specimen 4, the total elongation was higher than in BM, which is in accordance with a relatively fine grain in the weld. The opposite effect was exhibited in Specimen 5, where it was deemed that the main reason was the effect of the wormhole.

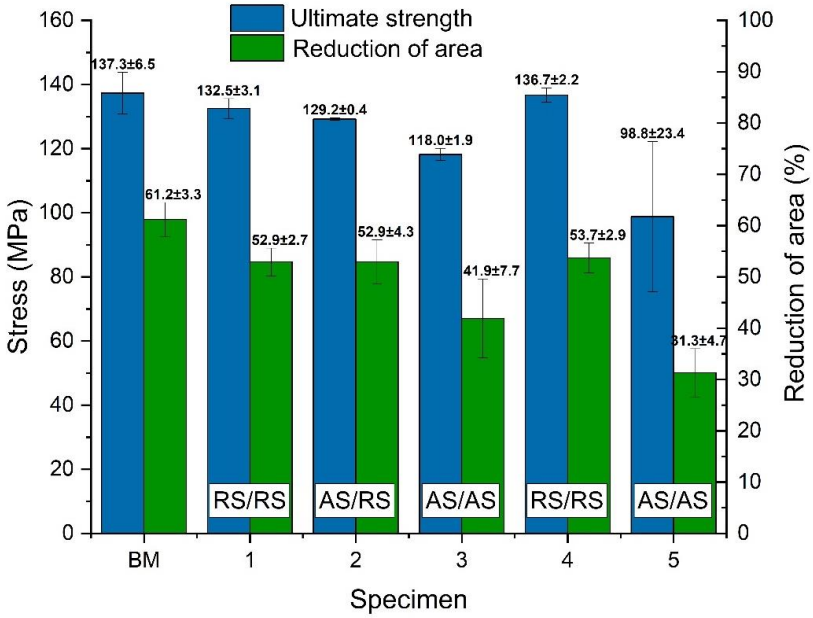

Figure 8. Tensile testing results (RS-reverse side; AS-advancing side).

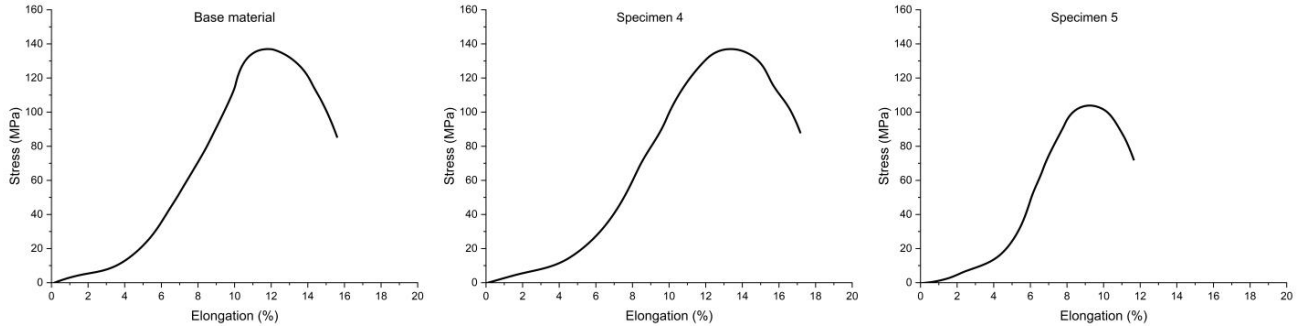

Figure 9. Stress-elongation curves for base material and Specimens 4 and 5.

Fracture surfaces of Specimens 1 and 4 are shown in Figures 10 and 11. In Specimen 1, a significant plastic deformation could be observed, particularly at the edges of the fractured surface and around the wormhole forms in the central-lower part of the specimen, marked by a white arrow Figure 10. Additionally, a quasi-cleavage fracture mode was present, exhibiting both cleavage and plastic deformation with clearly visible dimples. A very fine dimpled fracture surface, but one without a wormhole, was present in Specimen 4, as seen in Figure 11. A characteristic X-shaped fracture can be observed, common in

square cross-section tensile-tested specimens. The reductions of the area in Specimens 1 and 4 were similar; however, it is apparent that the dimples were finer in Specimen 1 (1 to 17 vs. 2 to 17 µm in Specimen 4), which is in accordance with the results of metallographic tests, Table 5. A wave-like morphology in the wormhole region, also marked by a white arrow, obtained in Specimen 1 was most likely the result of the stirring effect of the probe, where the waves represent the incremental material addition by the probe sides. This type of fracture surface morphology was also found by other researchers, including Oluwaseun in an AA5083 alloy [34], Gratecap et al. in an AA2017 alloy [35], and Chen et al. in an AA5456 alloy [36].

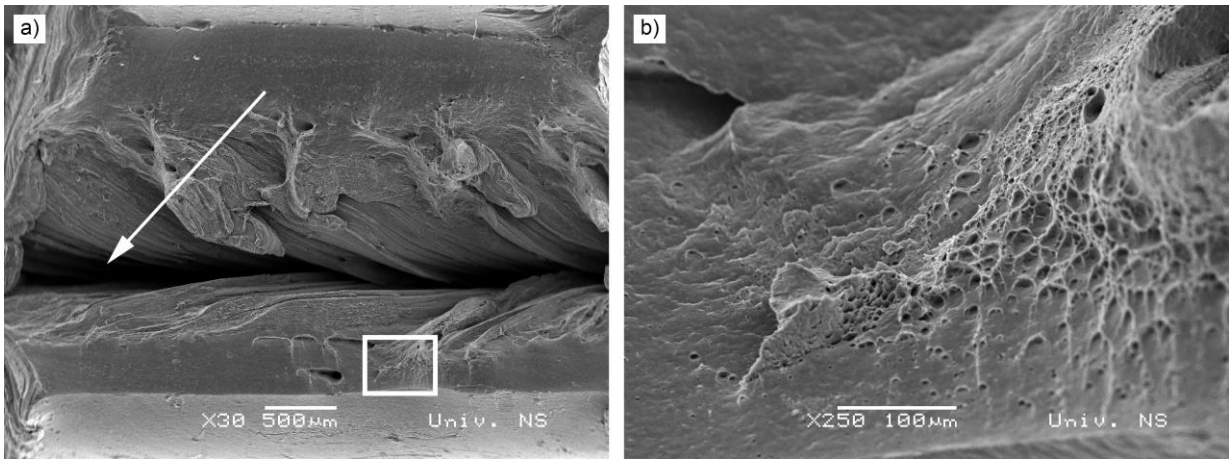

Figure 10. Tensile fracture surface of Specimen 1. (**a**) macro; (**b**) detail shown in white box.

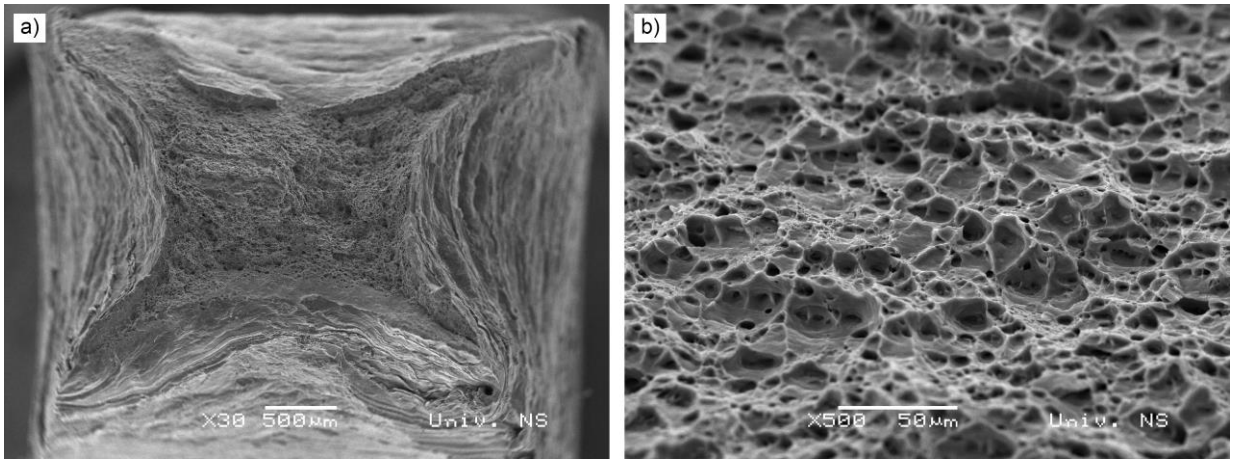

Figure 11. Tensile fracture surface of Specimen 4. (**a**) macro; (**b**) dimpled area in the center of the fracture.

3.4. Impact Energy Testing Results

Impact energy-testing results are shown in Figure 12. The highest crack initiation, crack propagation, the sum of them, and impact energy were obtained in Specimen 4, which replicates the results of tensile testing. This is the effect of the absence of a wormhole, unlike other specimens, particularly 1, 2 and 3, where there was a considerable drop in these values due to the centrally located wormhole (Specimen 1) or wormholes (Specimens 2 and 3). In Specimen 5, slightly lower values compared to Specimen 4 were obtained. This can be attributed to a marginally coarser grain in the nugget zone, as a result of a higher processing temperature. As the wormhole in this specimen was not located directly in the central weld zone, it can be assumed that its effect on impact energies was minor.

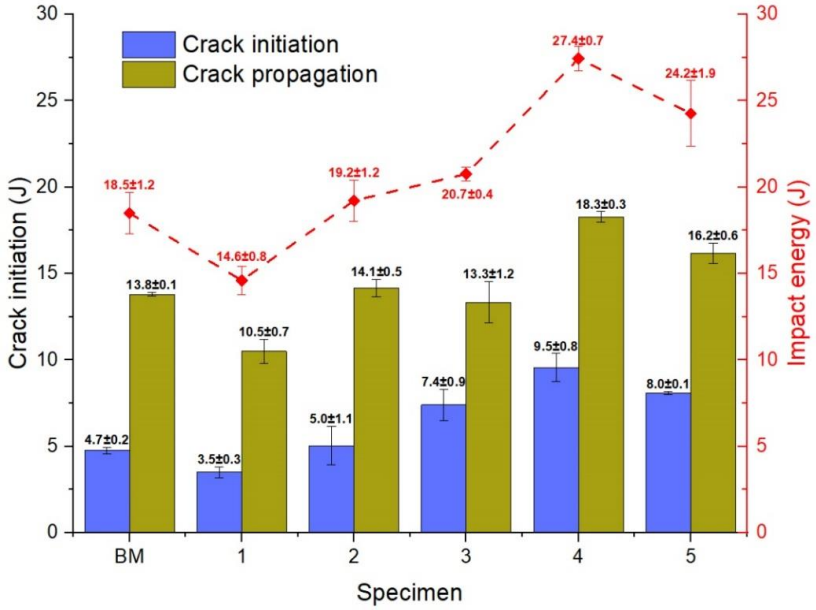

Figure 12. Impact energy testing results.

Compared to base metal, the impact energy effectiveness in Specimen 4 was 101%, 33%, and 48% higher, if crack initiation, crack propagation, and impact energy are considered, respectively. The main effect is the grain refinement in the nugget zone compared to the base metal, without the presence of a wormhole defect. This can be illustrated by the shape of the impact force versus fracture-time curves, as seen in Figure 13. Specimen 5, compared to base metal, had a considerably higher and longer chart, indicating that the maximal force was higher, and the duration of the fracture was also longer. On the other hand, all trends in terms of crack-initiation and crack-propagation energies, where the latter were higher, were the same as in base metal. However, the crack-initiation energy of Specimens (2–5) was roughly 1/3 of the whole impact energy. This was higher than for the BM and Specimen 1, where it was roughly 1/4. The latter was similar to the relatively brittle AA7049 alloy that was tested using an instrumented Charpy pendulum impact tester, reported in the work of Perovic et al. [37]. The greatest benefit of BTFSW pertained to impact energy, which was considerably higher than tensile performance. This in alignment with the results obtained in [6]. This could also be the result of the full elimination of root imperfections [38].

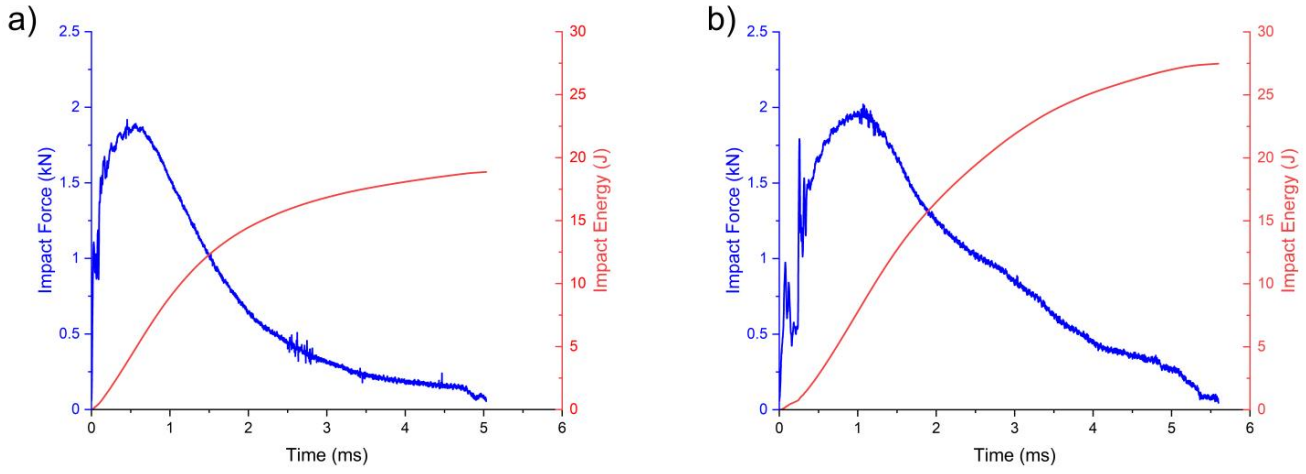

Figure 13. Impact force versus fracture time of (**a**) base metal; (**b**) Specimen 5 (line color corresponds to axis line color).

The fractured surfaces of Specimens 1 and 4 are shown in Figures 14 and 15. A similar dimpled fracture surface was obtained; however, shallower dimples were observed in Specimen 1, which reflects a lower ductility of Specimen 1. This is in accordance with the impact energy results shown in Figure 12.

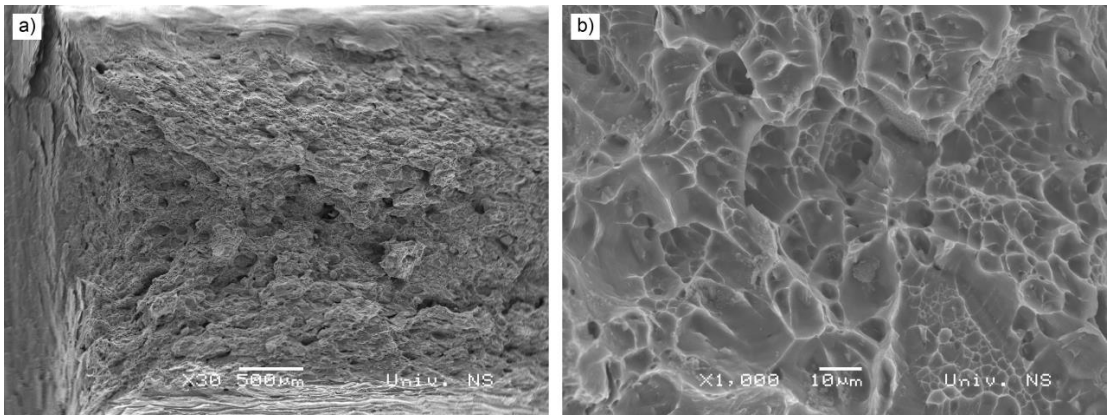

Figure 14. Impact energy fracture surface of Specimen 1. (**a**) macro; (**b**) dimpled surface.

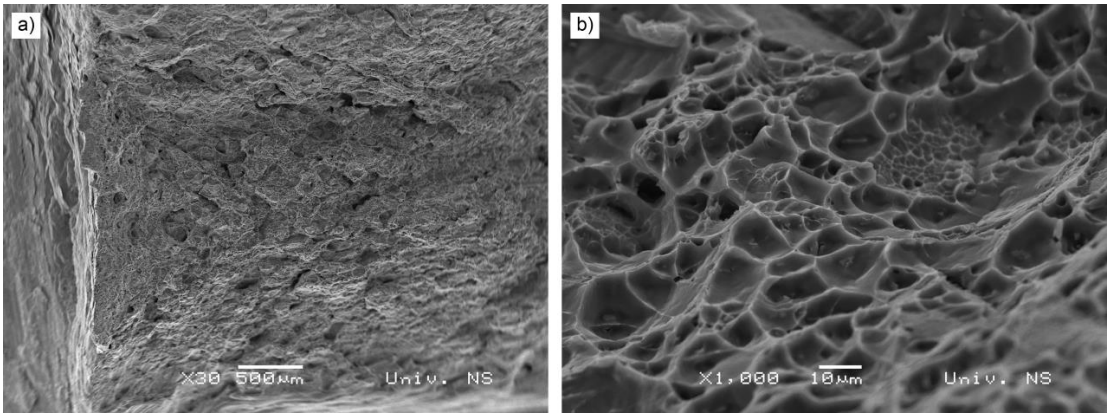

Figure 15. Impact energy fracture surface of Specimen 4. (**a**) macro; (**b**) dimpled surface.

3.5. Bend Testing

Bend testing results, over the bottom- and top-shoulder-formed surfaces, are shown in Table 6 and Figure 16. In Specimens 3 to 5, which were bent over the weld bottom surface, no cracks occurred. However, in Specimens 1 and 2, cracks occurred, probably because of wormholes. Subsequently, all specimens were bent to 180° without fracture, except for Specimen 1. When bent over the top surface, no cracks or fractures occurred. The main reason for the better performance when bent over the bottom of the welds was the location of long wormhole defects that were closer to the bottom, as was obtained in [6].

Table 6. Bend test results.

Specimen	Bending over the Bottom Surface		Bending over the Top Surface	
	First Crack°	Bend Test to 180°	First Crack°	Bend Test to 180°
1	13.6	Fracture	None	No fracture
2	93.1	No fracture	None	No fracture
3	None	No fracture	None	No fracture
4	None	No fracture	None	No fracture
5	None	No fracture	None	No fracture

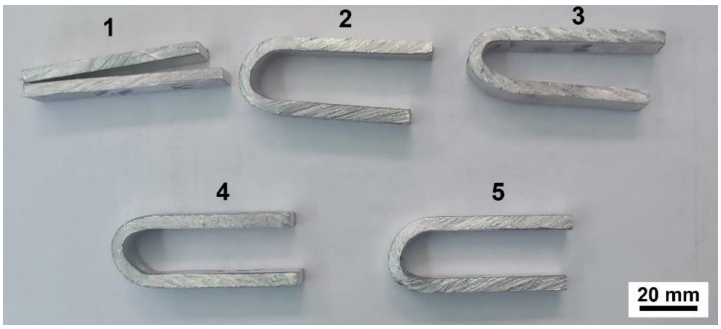

Figure 16. Specimens bent over the bottom surface.

The fracture surface of the bend-tested Specimen 1 is presented in Figure 17. The wormhole is clearly visible and played a major role in the premature failure (white arrow), which is a similar tendency to the tensile-tested specimen shown in Figure 10. A wave-like morphology of the wormhole sides was present as well, which was the result of the stirring effect of the probe. The visible wave-like morphology was obtained through incremental material addition of the probe sides during stirring. These tool marks are the result of unconsolidated material, formed by successive deposition of the material rotated and pushed around the tool pin. This occurred on the AS, when consolidation did not take place due to the loss of fluidity and poor forging pressure of the low-interference tool. These features were also found by Oluwaseun in an AA5083 alloy [34], Gratecap et al. in an AA2017 alloy [35], and Chen et al. in an AA5456 alloy [36]. Additionally, a quasi-cleavage fracture mode was present, exhibiting both cleavage and plastic deformation with clearly visible shear dimples, present on both sides of the wormhole, Figure 17b,c.

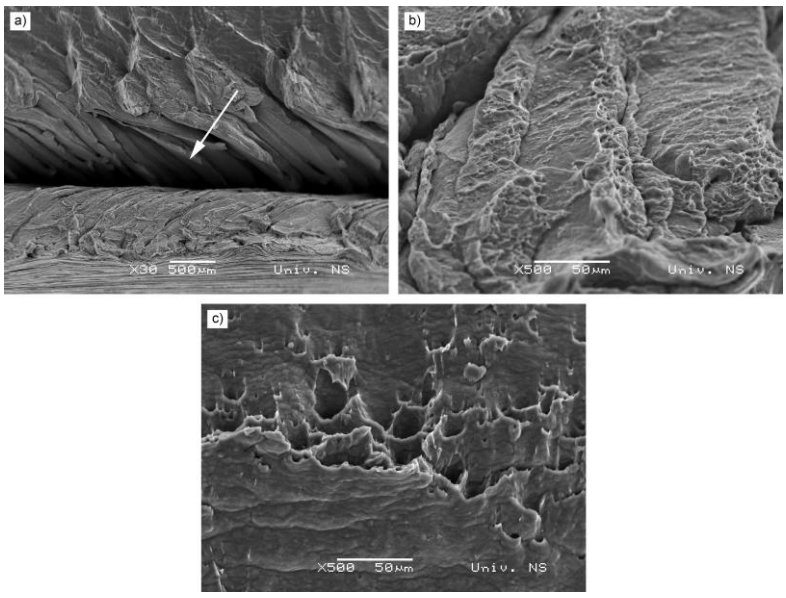

Figure 17. Bend fracture surface of Specimen 1: (**a**) macro depiction of the wormhole; (**b**) area under the wormhole; (**c**) area above the wormhole.

4. Conclusions

Based on the results and within the limitations of this study, the following conclusions can be drawn:

- The tool used, featuring simplified geometry to facilitate easier cleaning, proved to be effective in the FSW process.
- A higher interference influenced the rise in temperature due to a higher pressure imposed on the base metal.

- A rise in temperature caused a gradual reduction in wormhole occurrence, up to 0.4 mm. Over 0.4 mm, the wormhole occurs again.
- A higher interference and subsequent rise in temperature led to an increase in weld width-at-waist, the curvature of the weld became more pronounced, and grain-coarsening in the heat-affected zone and nugget was present.
- The grain-coarsening effect had a more adverse effect on tensile properties than the presence of wormholes, due to the longitudinal shape of the wormhole and an independent straining of the material around, without a significant reduction of the loaded area.
- An opposite effect was observed on impact strength, where the wormhole proved to have the dominant adverse effect over the grain refinement. Compared to other mechanical properties, the benefit of BTFSW was most pronounced in terms of impact strength performance.
- The most negative effect of wormholes was on bend-testing results, causing cracks and fractures in the specimen.
- The mechanical properties of optimal Specimen 4, obtained with BTFSW, are very similar to base metal in terms of tensile properties, however, the impact energy is considerably higher, which is the effect of a considerable grain refinement in the nugget zone.
- The optimal Specimen 4 fully complies with the most stringent acceptance level B listed in ISO 25239-5 standard, Specimens 3 and 5 with acceptance level C.

Author Contributions: S.B. wrote the paper and supervised the work; M.P., D.L.Z., M.D., N.K., P.J., M.H., D.R., S.R. and Z.L. performed the experiments; S.B. and D.L.Z. designed the experiments; S.B., M.H., D.R. and S.R. provided the resources. All authors have read and agreed to the published version of the manuscript.

Funding: This research received no external funding.

Data Availability Statement: Not applicable.

Acknowledgments: The authors gratefully acknowledge research support by the project entitled "Advanced materials, joining and allied technologies" in the Department of Production Engineering, Faculty of Technical Sciences Novi Sad, Serbia.

Conflicts of Interest: The authors declare no conflict of interest.

References

1. Mishra, R.S.; Ma, Z.Y. Friction Stir Welding and Processing. *Mater. Sci. Eng. R Reports* **2005**, *50*, 1–78. [CrossRef]
2. Mehta, K.P.; Badheka, V.J. A Review on Dissimilar Friction Stir Welding of Copper to Aluminum: Process, Properties, and Variants. *Mater. Manuf. Process.* **2016**, *31*, 233–254. [CrossRef]
3. Thomas, W.M.; Staines, D.G.; Norris, I.M.; Watts, E.R. Reversal Stir Welding—Preliminary Trials. *Weld. Des. Fabr.* **2003**, *76*, 32.
4. Sejani, D.; Li, W.; Patel, V. Stationary Shoulder Friction Stir Welding–Low Heat Input Joining Technique: A Review in Comparison with Conventional FSW and Bobbin Tool FSW. *Crit. Rev. Solid State Mater. Sci.* **2022**, *47*, 865–914. [CrossRef]
5. Goebel, J.; Reimann, M.; Norman, A.; dos Santos, J.F. Semi-Stationary Shoulder Bobbin Tool Friction Stir Welding of AA2198-T851. *J. Mater. Process. Technol.* **2017**, *245*, 37–45. [CrossRef]
6. Pecanac, M.; Labus Zlatanovic, D.; Kulundzic, N.; Dramicanin, M.; Lanc, Z.; Hadzistevic, M.; Radisic, S.; Balos, S. Influence of Tool and Welding Parameters on the Risk of Wormhole Defect in Aluminum Magnesium Alloy Welded by Bobbin Tool FSW. *MDPI Met.* **2022**, *12*, 14. [CrossRef]
7. Węglowski, M.S. Friction Stir Processing—State of the Art. *Arch. Civ. Mech. Eng.* **2018**, *18*, 114–129. [CrossRef]
8. Merah, N.; Azeel, M.A.; Hafiz, M.A.; Al-Badour, F.; Albinmousa, J.; Sorour, A.A. Friction Stir Processing Influence on Microstructure, Mechanical, and Corrosion Behavior of Steels: A Review. *Materials* **2021**, *14*, 5023. [CrossRef]
9. Mehta, K.P.; Vilaça, P. A Review on Friction Stir-Based Channeling. *Crit. Rev. Solid State Mater. Sci.* **2022**, *47*, 1–45. [CrossRef]
10. Drsno, I.Z.; Alnim, M.E.; Balos, S.; Sidjanin, L. Effect of Tunneling Defects on the Joint Strength Efficiency Obtained With Fsw Vpliv Tunelskih Napak Na U ˆ Inkovitost Trdnosti. *Mater. Technol.* **2014**, *48*, 491–496.
11. Jiang, W.; Miura, T.; Otsu, M.; Okada, M.; Matsumoto, R.; Yoshimura, H.; Muranaka, T. Development of Penetrating Tool Friction Stir Incremental Forming. *Mater. Trans.* **2019**, *60*, 2416–2425. [CrossRef]
12. Jiang, W.; Miura, T.; Otsu, M.; Okada, M.; Matsumoto, R.; Yoshimura, H.; Muranaka, T. Development of Friction Stir Incremental Forming Process Using Penetrating Tool. *Procedia Eng.* **2017**, *207*, 789–794. [CrossRef]

13. Wang, B.; Xu, L.; Guo, B.; Zhang, H. Process and Performance Characteristics of an Improved Friction-Stir Riveting Process. *J. Manuf. Process.* **2021**, *62*, 234–246. [CrossRef]
14. Liu, Z. Friction Stir Incremental Forming of AA7075-O Sheets: Investigation on Process Feasibility. *Procedia Eng.* **2017**, *207*, 783–788. [CrossRef]
15. Baffari, D.; Buffa, G.; Campanella, D.; Fratini, L. Design of Continuous Friction Stir Extrusion Machines for Metal Chip Recycling: Issues and Difficulties. *Procedia Manuf.* **2018**, *15*, 280–286. [CrossRef]
16. Thomas, W.M.; Johnson, K.I.; Wiesner, C.S. TWI ltd Friction Stir Welding—Recent Developments in Tool and Process Technologies. *Adv. Eng. Mater.* **2003**, *5*, 485–490. [CrossRef]
17. Fonda, R.W.; Bingert, J.F.; Colligan, K.J. Development of Grain Structure during Friction Stir Welding. *Scr. Mater.* **2004**, *51*, 243–248. [CrossRef]
18. Ahmed, M.M.Z.; Wynne, B.P.; Rainforth, W.M.; Threadgill, P.L. Quantifying Crystallographic Texture in the Probe-Dominated Region of Thick-Section Friction-Stir-Welded Aluminium. *Scr. Mater.* **2008**, *59*, 507–510. [CrossRef]
19. Fuse, K.; Badheka, V. Bobbin Tool Friction Stir Welding: A Review. *Sci. Technol. Weld. Join.* **2019**, *24*, 277–304. [CrossRef]
20. Hilgert, J. Knowledge Based Process Development of Bobbin Tool Friction Stir Welding. Ph.D. Thesis, Helmholtz-Zentrum Geesthacht Zentrum für Material- und Küstenforschung GmbH, Geesthacht, Germany, 2012.
21. Okamoto, K.; Sato, A.; Park, S.H.; Hirano, S. Microstructure and Mechanical Properties of FSWed Aluminum Extrusion with Bobbin Tools. *Mater. Sci. Forum* **2012**, *706–709*, 990–995. [CrossRef]
22. Sued, M.K.; Pons, D.J. Dynamic Interaction between Machine, Tool, and Substrate in Bobbin Friction Stir Welding. *Int. J. Manuf. Eng.* **2016**, *2016*, 8697453. [CrossRef]
23. Sued, M.K.; Pons, D.J.; Lavroff, J. Compresion Ratio Effects in Bobbin Friction Stir Welding. In Proceedings of the 10th International Symposium on Friction Stir Welding, Beijing, China, 20–22 May 2014.
24. Zhang, H.; Wang, M.; Zhang, X.; Yang, G. Microstructural Characteristics and Mechanical Properties of Bobbin Tool Friction Stir Welded 2A14-T6 Aluminum Alloy. *Mater. Des.* **2015**, *65*, 559–566. [CrossRef]
25. *ISO 25239-5;* Quality and Inspection Requirements. International Organization for Standardization: London, UK, 2020.
26. Amin, S.A.; Hanna, M.Y.; Mohamed, A.F. Experimental Study the Effect of Tool Design on the Mechanical Properties of Bobbin Friction Stir Welded 6061-T6 Aluminum Alloy. *Al-Khwarizmi Eng. J.* **2018**, *14*, 1–11. [CrossRef]
27. Labus Zlatanovic, D.; Balos, S.; Bergmann, J.P.; Rasche, S.; Pecanac, M.; Goel, S.; Zlatanovic, D.L.; Balos, S.; Bergmann, J.P.; Rasche, S.; et al. Influence of Tool Geometry and Process Parameters on the Properties of Friction Stir Spot Welded Multiple (AA 5754 H111) Aluminium Sheets. *Materials* **2021**, *14*, 1157. [CrossRef]
28. Fuse, K. Investigation of Bobbin Tool Friction Stir Welding. Ph.D. Thesis, Pandit Deendayal Petroleum University, Gujarat, India, 2021.
29. Dickerson, T.L.; Przydatek, J. Fatigue of Friction Stir Welds in Aluminium Alloys That Contain Root Flaws. *Int. J. Fatigue* **2003**, *25*, 1399–1409. [CrossRef]
30. Leonard, A.J.; Lockyer, S.A. Flaws in Friction Stir Welds. In Proceedings of the 4th International Symposium on Friction Stir Welding, Park City, UT, USA, 14–16 May 2003.
31. Threadgilll, P.L.; Leonard, A.J.; Shercliff, H.R.; Withers, P.J. Friction Stir Welding of Aluminium Alloys. *Int. Mater. Rev.* **2009**, *54*, 49–93. [CrossRef]
32. Shen, Z.; Yang, X.; Yang, S.; Zhang, Z.; Yin, Y. Microstructure and Mechanical Properties of Friction Spot Welded 6061-T4 Aluminum Alloy. *Mater. Des.* **2014**, *54*, 766–778. [CrossRef]
33. Sahu, P.K.; Vasudevan, N.P.; Das, B.; Pal, S. Assessment of Self-Reacting Bobbin Tool Friction Stir Welding for Joining AZ31 Magnesium Alloy at Inert Gas Environment. *J. Magnes. Alloy.* **2019**, *7*, 661–671. [CrossRef]
34. Dada, O.J. Fracture Mechanics and Mechanical Behaviour in AA5083-H111 Friction Stir Welds. *Sci. African* **2020**, *8*, e00265. [CrossRef]
35. Gratecap, F.; Girard, M.; Marya, S.; Racineux, G. Exploring Material Flow in Friction Stir Welding: Tool Eccentricity and Formation of Banded Structures. *Int. J. Mater. Form.* **2012**, *5*, 99–107. [CrossRef]
36. Chen, H.B.; Yan, K.; Lin, T.; Chen, S.B.; Jiang, C.Y.; Zhao, Y. The Investigation of Typical Welding Defects for 5456 Aluminum Alloy Friction Stir Welds. *Mater. Sci. Eng. A* **2006**, *433*, 64–69. [CrossRef]
37. Perović, M.; Baloš, S.; Kozak, D.; Bajić, D.; Vuherer, T. Utjecaj Kinematičkih Faktora Zavarivanja Trenjem Miješanjem Na Karakteristike Zavarenog Spoja Kovanih Ploča Od Legure Aluminija EN AW 7049 A. *Teh. Vjesn.* **2017**, *24*, 723–728. [CrossRef]
38. Wang, G.Q.; Zhao, Y.H.; Tang, Y.Y. Research Progress of Bobbin Tool Friction Stir Welding of Aluminum Alloys: A Review. *Acta Metall. Sin.* **2020**, *33*, 13–29. [CrossRef]